AIAA JOURNAL
Vol. 41, No. 5, May 2003

Low-Reynolds-Number Turbulent Flows in Locally Constricted Conduits: A Comparison Study

Zhe Zhang* and Clement Kleinstreuer†
North Carolina State University, Raleigh, North Carolina 27695

In numerous internal flow systems the velocity field can undergo all flow regimes, that is, from laminar, via transitional, to fully turbulent. Considering two test conduits with local constrictions, four turbulence models, with an emphasis on low-Reynolds-number (LRN) turbulence models, were compared and evaluated. The objective was to identify a readily available LRN turbulence model with which incompressible laminar-to-turbulent velocity and pressure fields in complex three-dimensional conduits can be directly computed. The comparison study revealed that the renormalization group (RNG) k–ε and Menter k–ω models amplify the flow instabilities after tubular constrictions and hence fail to capture the laminar flow behavior at low Reynolds numbers. The LRN k–ε model fails to simulate the transition to turbulent flow, and it requires relatively high computational resources because of the slower convergence. The LRN k–ω model adopted for complex three-dimensional tubular flows in this study appears to be capable of reproducing the behavior of laminar, transitional, and fully turbulent flows. Moreover, the LRN k–ω model predicts the maximum turbulence fluctuations quite well. Hence, it is concluded that the LRN k–ω model is suitable for simulating laminar-transitional-turbulent flows in constricted tubes, such as the human upper airways, stenosed blood vessels, obstructed pipes, etc.

Nomenclature

D = diameter of unobstructed tube
k = turbulence kinetic energy
p = mean static pressure
Q_{in} = inspiratory flow rate at the mouth
R = radius of unobstructed tube
R_T = turbulence Reynolds number
Re = Reynolds number at the inlet
s_{ij} = strain-rate tensor
u = axial velocity
u_i = mean velocity in tensor notation
u_{in} = mean velocity at the inlet
u_τ = friction velocity, $u_\tau = \sqrt{\tau_w/\rho_w}$
x_i = position vector in tensor notation
y^+ = dimensionless distance from wall, sublayer scaled distance, $y^+ = u_\tau y/\nu$
ε = turbulence dissipation rate
μ = molecular viscosity
μ_T = eddy viscosity
ν = kinetic molecular viscosity, $\nu = \mu/\rho$
ν_T = kinetic eddy viscosity, $\nu_T = \mu_T/\rho$
ρ = fluid density
τ_{ij} = Reynolds-stress tensor
ω = pseudovorticity, dissipation per unit turbulence kinetic energy

Introduction

IN numerous natural and industrial systems entrance flows are laminar and then, via a transitional region, become turbulent as a result of local area reductions. Examples include the oral airways from mouth to trachea, stenosed blood vessels, Venturi meters, ducts of propulsion systems, and pipes with flow nozzles, valves, etc. Researchers relying on the standard k–ε turbulence model or its modified versions to simulate incompressible Newtonian fluid flow covering the laminar–turbulent–laminar flow regimes usually failed to match experimental data sets.[1–6] The k–ω turbulence model developed by Wilcox[7] and the combined k–ω (inner) and k–ε (outer) turbulence model of Menter[8] are interesting improvements over the basic k–ε model. However, all standard turbulence models assume fully developed turbulent flows; hence, one has to turn to their internal low-Reynolds-number flow versions for simulating laminar-to-turbulent flows, say, in locally constricted conduits.

Jones and Launder[9] introduced the first version of the low-Reynolds-number (LRN) k–ε model, where the so-called LRN function is chosen instead of the wall function approach such that the near-wall damping effects can be simulated because of its more rigorous near-wall treatment of turbulent quantities. Launder and Sharma,[10] Lam and Bremhorst,[11] and Chien[12] exemplified most of the features incorporated in the model's viscous damping function. However, as reviewed by Kral,[13] the differences in flow predictions of five LRN k–ε models were not that significant. Recently, Radmehr and Patankar[14] reviewed and evaluated LRN k–ε turbulence models and concluded that they can predict qualitative aspects of transition but fail to predict the quantitative aspects of transition correctly. Wilcox[7] illustrated that the k–ε model is difficult to implement for transitional flow. He pointed out that the k–ω model with low-Reynolds-number effect corrections, that is, the LRN k–ω turbulence model, is expected to predict transitional flow quite well.

In this paper we consider four widely used turbulence models, that is, the RNG k–ε, Menter k–ω, LRN k–ε, and LRN k–ω model. However, the first two should be more appropriate for high-Reynolds-number flows and hence are only considered in the first case study. The two conduits selected are a tube with a smooth sinusoidal constriction, for which experimental data sets are available, and the human oral airways, where the larynx causes a major flow restriction and hence the onset to turbulence for elevated inhalation rates. Although the two geometric test cases selected represent laboratory and respiratory conduits, submodels and solution method are also applicable to aerodynamic systems, for example, part fuel-injected internal combustion engines[15] and airbreathing propulsion inlet systems.[16]

Theory

The two internal laminar-to-turbulent flow systems under consideration are depicted in Fig. 1. As shown in Fig. 1a, the axisymmetric conduit exhibits a 75% area reduction whose shape is represented

---

Received 18 April 2002; revision received 9 September 2002; accepted for publication 30 November 2002.

*Research Assistant Professor, Department of Mechanical and Aerospace Engineering.

†Professor, Department of Mechanical and Aerospace Engineering; ck@eos.ncsu.edu.

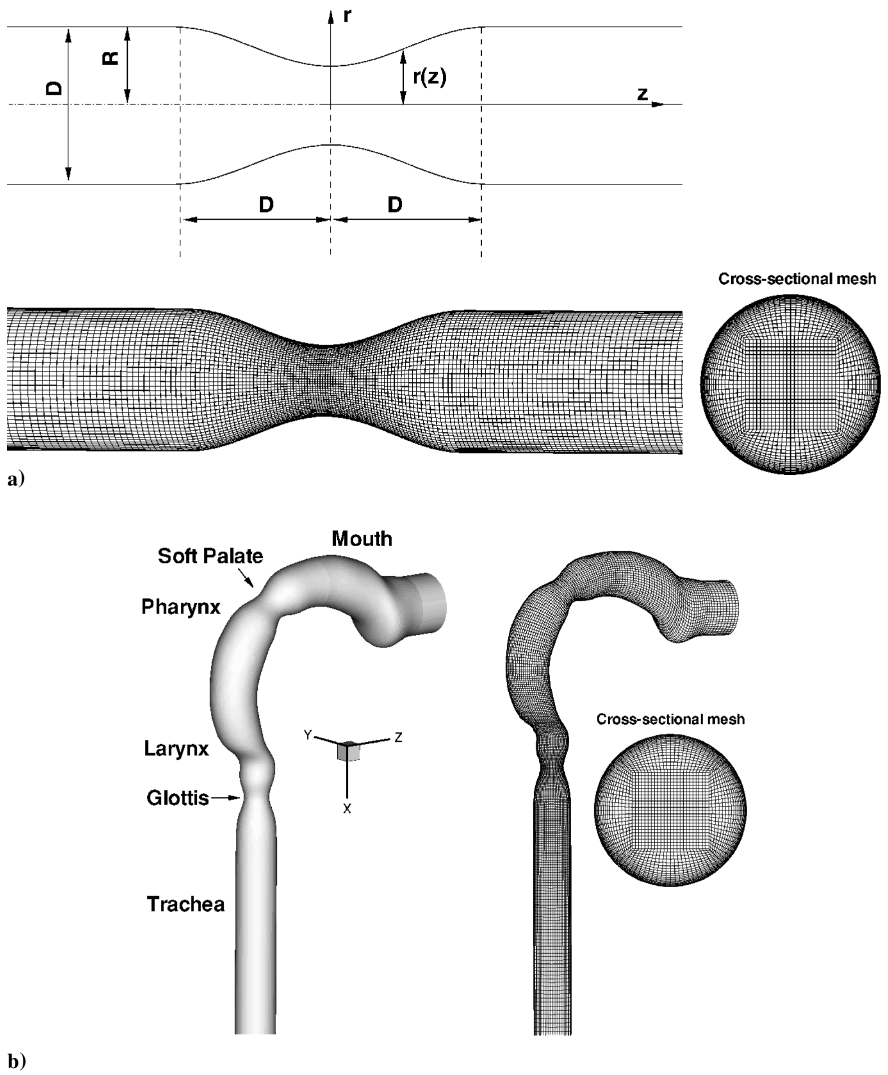

Fig. 1 Schematic diagrams and computational meshes for a) a tube with an axisymmetric constriction and b) a human oral airway model.

by a cosine function as

$$r(z) = \begin{cases} R - \dfrac{R}{2}\cos\left(\dfrac{\pi z}{2D}\right) & \text{if} \quad |z| \le D \\ R & \text{if} \quad |z| > D \end{cases} \tag{1}$$

The human oral airway depicted in Fig. 1b includes the oral cavity (mouth), pharynx, larynx, and trachea. Figure 2 provides the diameter and Reynolds-number variations for typical inhalation flow rates along the oral airway from mouth to trachea. It is assumed that the incompressible Newtonian fluid flow is steady. Thus, the governing equations are as follows.

Continuity:

$$\frac{\partial u_i}{\partial x_i} = 0 \tag{2}$$

Momentum:

$$\frac{\partial u_i}{\partial t} + u_j \frac{\partial u_i}{\partial x_j} = -\frac{1}{\rho}\frac{\partial p}{\partial x_i} + \frac{\partial}{\partial x_j}\left[(\nu + \nu_T)\left(\frac{\partial u_i}{\partial x_j} + \frac{\partial u_j}{\partial x_i}\right)\right] \tag{3}$$

The different turbulence kinetic energy k equations and pseudovorticity ω equations, or the dissipation-rate ε equation, represent the four turbulence models.

LRN k–ω model:

$$\frac{\partial k}{\partial t} + u_j \frac{\partial k}{\partial x_j} = \tau_{ij}\frac{\partial u_i}{\partial x_j} - \beta^* k\omega + \frac{\partial}{\partial x_j}\left[(\nu + \sigma_k \nu_T)\frac{\partial k}{\partial x_j}\right] \tag{4}$$

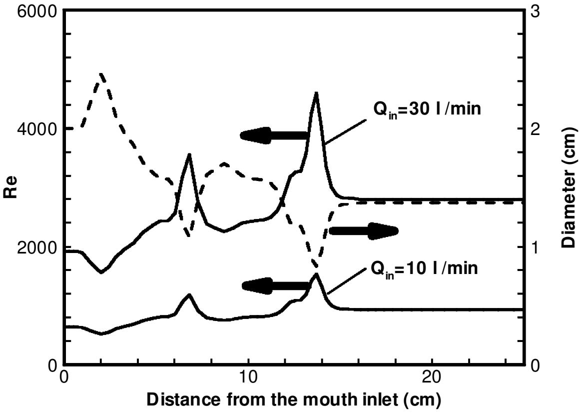

Fig. 2 Variations of Reynolds number and cross-sectional diameter in the oral-airway model.

$$\frac{\partial \omega}{\partial t} + u_j \frac{\partial \omega}{\partial x_j} = \alpha \frac{\omega}{k}\tau_{ij}\frac{\partial u_i}{\partial x_j} - \beta\omega^2 + \frac{\partial}{\partial x_j}\left[(\nu + \sigma_\omega \nu_T)\frac{\partial \omega}{\partial x_j}\right] \tag{5}$$

where the turbulent viscosity is given as $\nu_T = c_\mu f_\mu k/\omega$ and the function f_μ is defined as

$$f_\mu = \exp\left[-3.4/(1 + R_T/50)^2\right] \quad \text{with} \quad R_T = \rho k/(\mu\omega)$$

The other coefficients in the preceding equations are

$$C_\mu = 0.09 \tag{6a}$$

$$\alpha = 0.555 \tag{6b}$$

$$\beta = 0.8333 \tag{6c}$$

$$\beta^* = 1 \tag{6d}$$

$$\sigma_k = 0.5 \tag{6e}$$

$$\sigma_\omega = 0.5 \tag{6f}$$

LRN k–ε model:

$$\frac{\partial k}{\partial t} + u_j\frac{\partial k}{\partial x_j} = \tau_{ij}\frac{\partial u_i}{\partial x_j} - \varepsilon + \frac{\partial}{\partial x_j}\left[(\nu + \sigma_k\nu_T)\frac{\partial k}{\partial x_j}\right] + L_k \tag{7}$$

$$\frac{\partial \varepsilon}{\partial t} + u_j\frac{\partial \varepsilon}{\partial x_j} = \alpha\frac{\varepsilon}{k}\tau_{ij}\frac{\partial u_i}{\partial x_j} - \beta f_2\frac{\varepsilon^2}{k} + \frac{\partial}{\partial x_j}\left[(\nu + \sigma_\varepsilon\nu_T)\frac{\partial \varepsilon}{\partial x_j}\right] + L_\varepsilon \tag{8}$$

where $\nu_T = c_\mu f_\mu k^2/\varepsilon$, $f_\mu = \exp[-3.4/(1 + R_T/50)^2]$ with $R_T = \rho k^2/(\mu\varepsilon)$;

$$f_2 = 1 - 0.3\exp\left(-R_T^2\right) \tag{9}$$

$$L_k = 2\nu\left(\frac{\partial\sqrt{k}}{\partial x_j}\right)^2 \tag{10a}$$

$$L_\varepsilon = 2\nu\nu_T\left(\frac{\partial^2 u_i}{\partial x_j \partial x_i}\right)^2 \tag{10b}$$

$$C_\mu = 0.09 \tag{11a}$$

$$\alpha = 1.44 \tag{11b}$$

$$\beta = 1.92 \tag{11c}$$

$$\sigma_k = 1 \tag{11d}$$

$$\sigma_\varepsilon = 1.3 \tag{11e}$$

For the Menter k–ω model the turbulence kinetic energy equation is the same as Eq. (4). However, the pseudovorticity equation reads

$$\frac{\partial \omega}{\partial t} + u_j\frac{\partial \omega}{\partial x_j} = \alpha\frac{\omega}{k}\tau_{ij}\frac{\partial u_i}{\partial x_j} - \beta\omega^2 + \frac{\partial}{\partial x_j}\left[(\nu + \sigma_\omega\nu_T)\frac{\partial \omega}{\partial x_j}\right] + 2(1 - F)\sigma_{\omega_2}\frac{\nu_T}{k}\frac{\partial k}{\partial x_j}\frac{\partial \omega}{\partial x_j} \tag{12}$$

where $\nu_T = c_\mu k/\omega$. The constants of the model are calculated from the original k–ω model ϕ_1 and transformed k–ε model ϕ_2 depending on F through the relation

$$\phi = F\phi_1 + (1 - F)\phi_2 \tag{13}$$

where

$$F = \tanh(a^4) \tag{14}$$

$$a = \min\left\{\max\left[\frac{k^{0.5}}{\omega y}, \frac{500C_\mu\mu}{\rho\omega y^2}\right], \frac{4\rho k}{A\sigma_{\omega_2}y^2}\right\} \tag{15}$$

$$A = \max\left[\frac{2\mu_T}{C_\mu\sigma_{\omega_2}k}\frac{\partial k}{\partial x_j}\frac{\partial \omega}{\partial x_j}, 10^{-20}\right] \tag{16}$$

In these formulas, y is the distance to the nearest wall. The constants of set 1 (ϕ_1) (Wilcox model) are the same as in Eqs. (6a–6f), and the constants of set 2 (ϕ_2) (standard k–ε) are

$$C_{\mu 2} = 0.09 \tag{17a}$$

$$\alpha_2 = 0.555 \tag{17b}$$

$$\beta_2 = 1.92 \tag{17c}$$

$$\beta_2^* = 1.0 \tag{17d}$$

$$\sigma_{k2} = 1.0 \tag{17e}$$

$$\sigma_{\omega 2} = 1.22 \tag{17f}$$

RNG k–ε model:

$$\frac{\partial k}{\partial t} + u_j\frac{\partial k}{\partial x_j} = \tau_{ij}\frac{\partial u_i}{\partial x_j} - \varepsilon + \frac{\partial}{\partial x_j}\left[(\nu + \sigma_k\nu_T)\frac{\partial k}{\partial x_j}\right] \tag{18a}$$

$$\frac{\partial \varepsilon}{\partial t} + u_j\frac{\partial \varepsilon}{\partial x_j} = (\alpha - \alpha_{\text{RNG}})\frac{\varepsilon}{k}\tau_{ij}\frac{\partial u_i}{\partial x_j} - \beta^*\frac{\varepsilon^2}{k} + \frac{\partial}{\partial x_j}\left[(\nu + \sigma_\varepsilon\nu_T)\frac{\partial \varepsilon}{\partial x_j}\right] \tag{18b}$$

where

$$\nu_T = \frac{c_\mu k^2}{\varepsilon} \tag{19a}$$

$$\alpha_{\text{RNG}} = \frac{\eta(1 - \eta/\eta_0)}{1 + \beta\eta^3} \tag{19b}$$

$$\eta = \left(\frac{P_s}{\mu_r}\right)^{0.5}\frac{k}{\varepsilon} \tag{19c}$$

$$P_s = \frac{Sk}{\varepsilon} \tag{20a}$$

$$S = (2s_{ij}s_{ij})^{\frac{1}{2}} \tag{20b}$$

$$C_\mu = 0.09 \tag{21a}$$

$$\alpha = 1.42 \tag{21b}$$

$$\beta = 0.012 \tag{21c}$$

$$\beta^* = 1.68 \tag{21d}$$

$$\eta_0 = 4.38 \tag{21e}$$

$$\sigma_k = 1.39 \tag{21f}$$

$$\sigma_\varepsilon = 1.39 \tag{21g}$$

In all case studies uniform velocity profiles and zero pressure were prescribed at the inlet and outlet, respectively. The initial values for k, ω, or ε at the inlet were assigned in form of empirical relations, that is,

$$k = 1.5(I \times u_{\text{in}})^2, \qquad \omega = k^{0.5}/0.3D \qquad \text{or} \qquad \varepsilon = k^{1.5}/0.3D \tag{22}$$

where I is the turbulence intensity, usually taken as 0.037, and D is the diameter of the inlet tube.

Numerical Method

The numerical solutions of the continuity and momentum equations as well as the k and ω or ε equations were carried out using a user-enhanced commercial finite volume based program CFX4.4.[17] The numerical program uses a structured, multiblock, body-fitted coordinate discretization scheme. In the present simulation the pressure implicit splitting of operators (PISO) algorithm with underrelaxation was employed to solve the flow equations. All variables, including velocity components, pressure, and turbulence quantities, were located at the centroids of the control volumes. An improved Rhie–Chow interpolation method was employed to obtain the velocity components, pressure, and turbulence variables on the control volume faces from those at the control volume centers. A higher-order upwind differencing scheme, which is second-order accurate

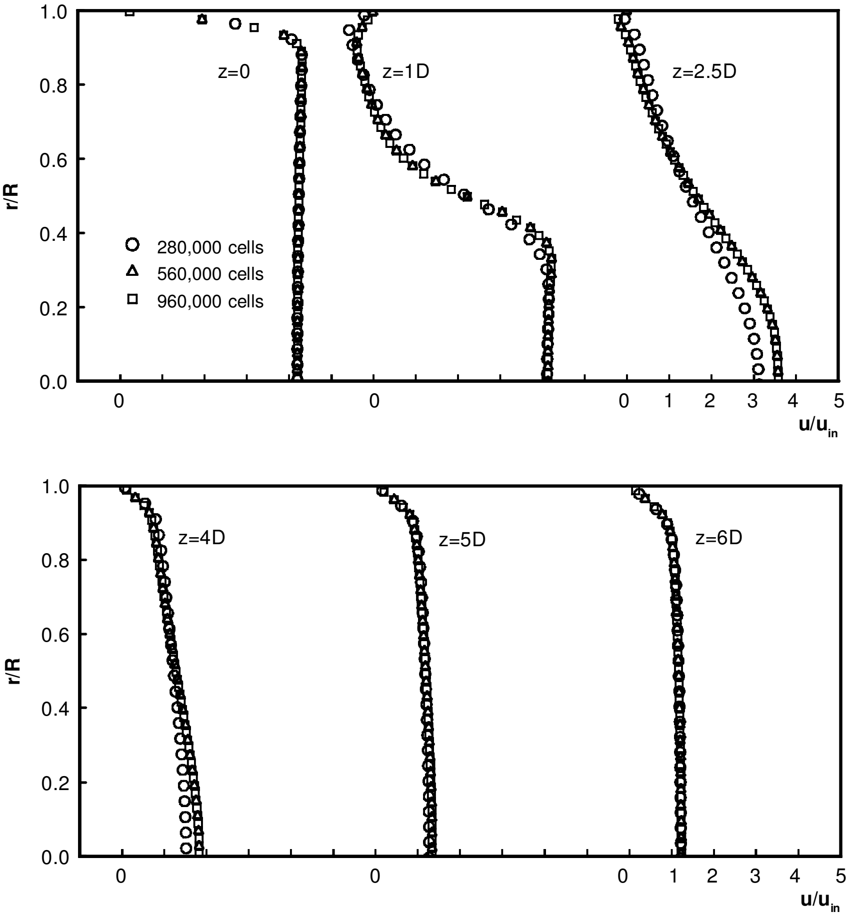

Fig. 3 Grid-refinement test for the axisymmetric constricted tube case. The profiles were obtained using the LRN k–ω model.

in space, was used to model the advective terms of the transport equations. The sets of linearized and discretized equations for all variables were solved using the Block Stone's method.

The computational meshes (cf. Fig. 1) were generated with CFX Build4. A very dense mesh was generated in the near-wall region. Specifically, the thickness of the near-wall cells was chosen to fully contain the viscous sublayers and to resolve any geometric features present there. As a requirement of LRN turbulence modeling, the first grid point above the wall was given a value of $y^+ \leq 1$, where $y^+ = u_\tau y/\nu$ is the inner variable or sublayer-scaled distance, and this criterion is strictly maintained for all computations. The mesh topology was determined by refining the mesh until grid independence of the flow field solution was achieved. For example, Fig. 3 shows one typical grid-refinement case for the constricted tube with a 75% area reduction at an inlet Reynolds number of $Re = 2 \times 10^3$. Grids consisting of about 280,000, 560,000, and 960,000 cells were tested. Almost no variation in the mean velocity profiles after the throat can be observed between the two highest grid density solutions. The final mesh size of the constricted tube model used was about 560,000 cells. The mesh of the oral-airway model contained about 640,000 cells. The computations were performed on an SGI Origin 2400 workstation with 32GB RAM and multiple 450 MHz CPUs. The steady-state solution of the flowfield was assumed converged when the dimensionless mass residual (total mass residual)/(mass flow rate) $< 10^{-3}$. The convergence of the turbulence quantities (k, ω, or ε) was monitored as well. Typical run times for the simulations employing the k–ω models on four parallel processors ranged from 15 to 30 h for the constricted tube and 30 to 50 h for the oral-airway model. The run times with the k–ε models differed by a factor of one-half to three, depending on the inlet Reynolds number.

Results and Discussion

Developing Turbulent Flow in Tubes with Sinusoidal Constrictions

The simulation of flow in a rigid tube with an axisymmetric constriction (see Fig. 1a) was performed first to assess the four widely used turbulence models [see Eqs. (4–21)]. Ahmed and Giddens[18,19] conducted experimental measurements focusing on the velocity fields in the neighborhood of the same axisymmetric constriction at inlet Reynolds numbers of 5×10^2 to 2×10^3. Figure 4 shows the comparisons of computed velocity profiles using the LRN k–ε, LRN k–ω, RNG k–ε, and Menter k–ω models for an inlet Reynolds number of $Re = 5 \times 10^2$. It can be seen that both LRN k–ε and LRN k–ω models agree well with the experimental profiles at the six stations; in fact, LRN k–ω and LRN k–ε modeling results are identical except in the throat at $z = 0$. In contrast, the performances of the RNG k–ε and Menter k–ω models deteriorate greatly outside the throat region, that is, $z > 1D$, although the Menter k–ω model behaves better than the RNG k–ε model in the tube section $0 \leq z/D \leq 4$. It is clear that the flow instabilities after the throat are excessively amplified in the RNG k–ε and Menter k–ω models for low-Reynolds-number flows. Both RNG k–ε and Menter k–ω models predict poststenotic turbulence as indicated by the blunt velocity profiles. In fact, the flow fluctuations tend to be very weak, and no poststenotic turbulence was observed at $Re = 5 \times 10^2$ in the experimental study.[19] In summary, both Menter k–ω and RNG k–ε models fail to treat the low-Reynolds-number laminar-to-transitional flow regimes.

The change in centerline velocity as a function of axial position is given in Fig. 5 for an inlet $Re = 2 \times 10^3$. Distinct vortex shedding and turbulent wake fields after the constriction were observed in the experiments. It is seen that the centerline velocity remains constant until $z = 2D$ and then decreases rapidly as a result of the area expansion and transition to turbulent flow in conjunction with the large-scale momentum transfer. The LRN k–ε model completely fails to predict the onset of turbulence in this case, whereas the prediction with the LRN k–ω model is consistent with the laboratory measurements. The profiles obtained with the Menter k–ω model follow closely the one obtained with the LRN k–ω model and hence the experimental data points in this moderate-Reynolds-number case. More detailed comparisons of the

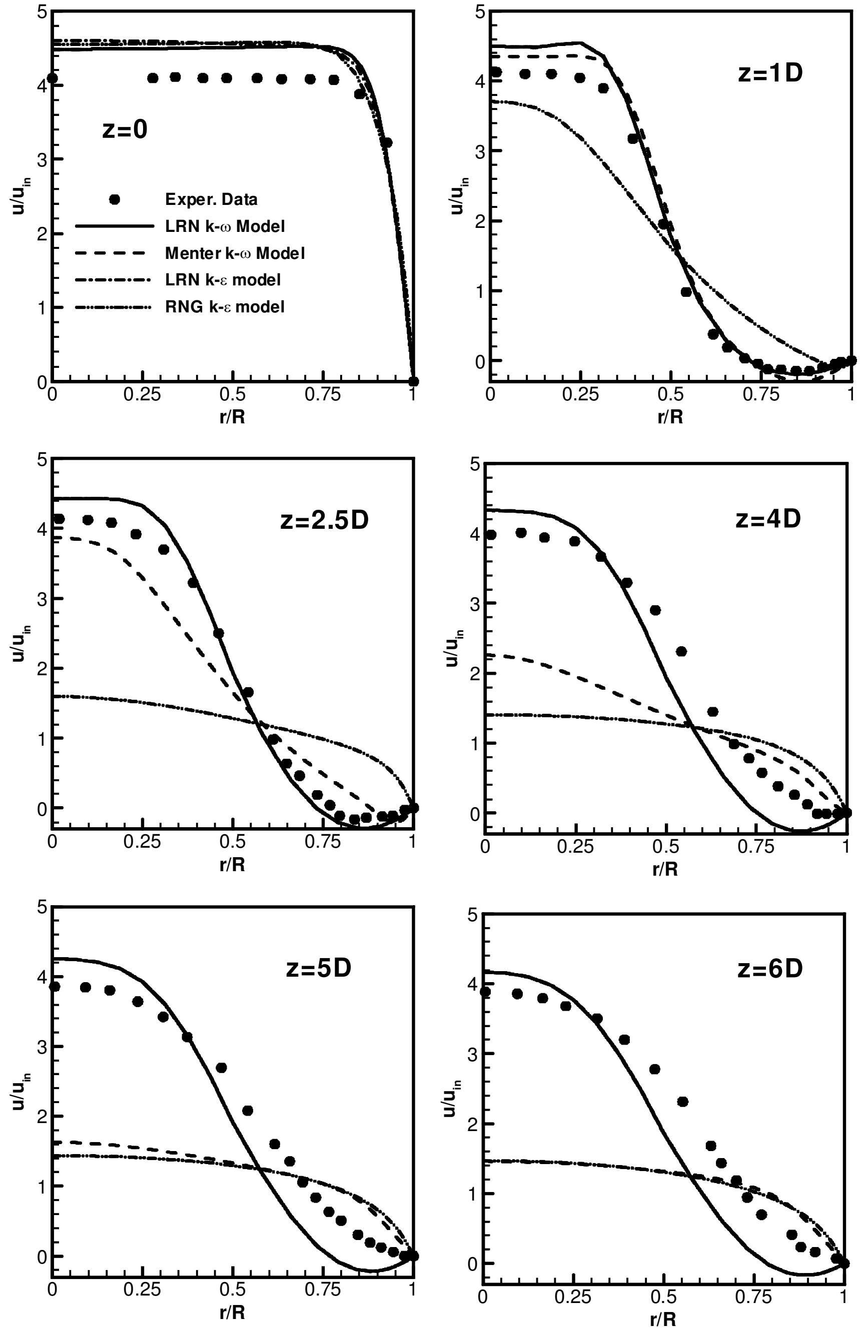

Fig. 4 Comparison of predicted axial velocity profiles at different axial locations for a 75% area reduction at $Re = 5 \times 10^2$ with the experimental measurements of Ahmed and Giddens.[18]

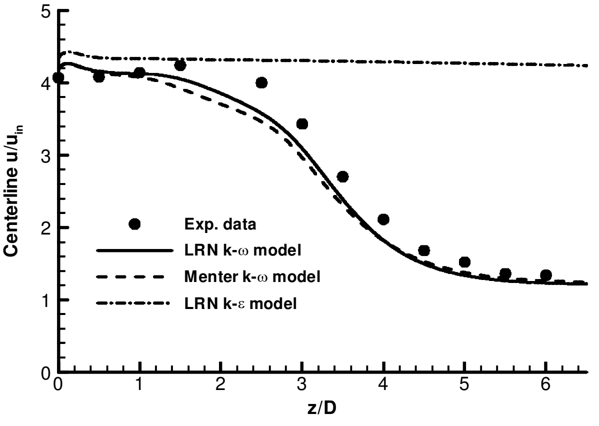

Fig. 5 Comparison of computed centerline velocity for the constricted tube at $Re = 2 \times 10^3$ with experimental measurements of Ahmed and Giddens.[18]

computed axial velocity profiles with the experimental measurements for $Re = 2 \times 10^3$ are given in Fig. 6. Comparisons with the LRN k–ε and RNG k–ε models are omitted because of their poor performance. Clearly, the LRN k–ω model captures very well the flow characteristics after the stenosis, including 1) the nearly uniform flow at the throat, 2) the development of the shear layer and the recirculatory flow before $z = 4D$, and 3) the occurrence of transition to turbulence indicated by the rather blunt velocity profile after $z = 5D$ caused by the redistribution of the kinetic energy of the flow over most of the cross section. Some differences in velocity magnitudes can be observed at stations $z = 2.5D$, $4D$, and $5D$. This can be attributed to the increasing experimental uncertainty in regions where the velocity profiles change rapidly as a result of the local onset of turbulence.

The performances of the LRN k–ω and Menter k–ω models are further evaluated for the intermediate-Reynolds-number case ($Re = 10^3$), as shown in Fig. 7. The Reynolds number of 10^3 is in the vicinity of the critical Reynolds number at which the shear layer becomes unstable and transition to turbulence can occur after the

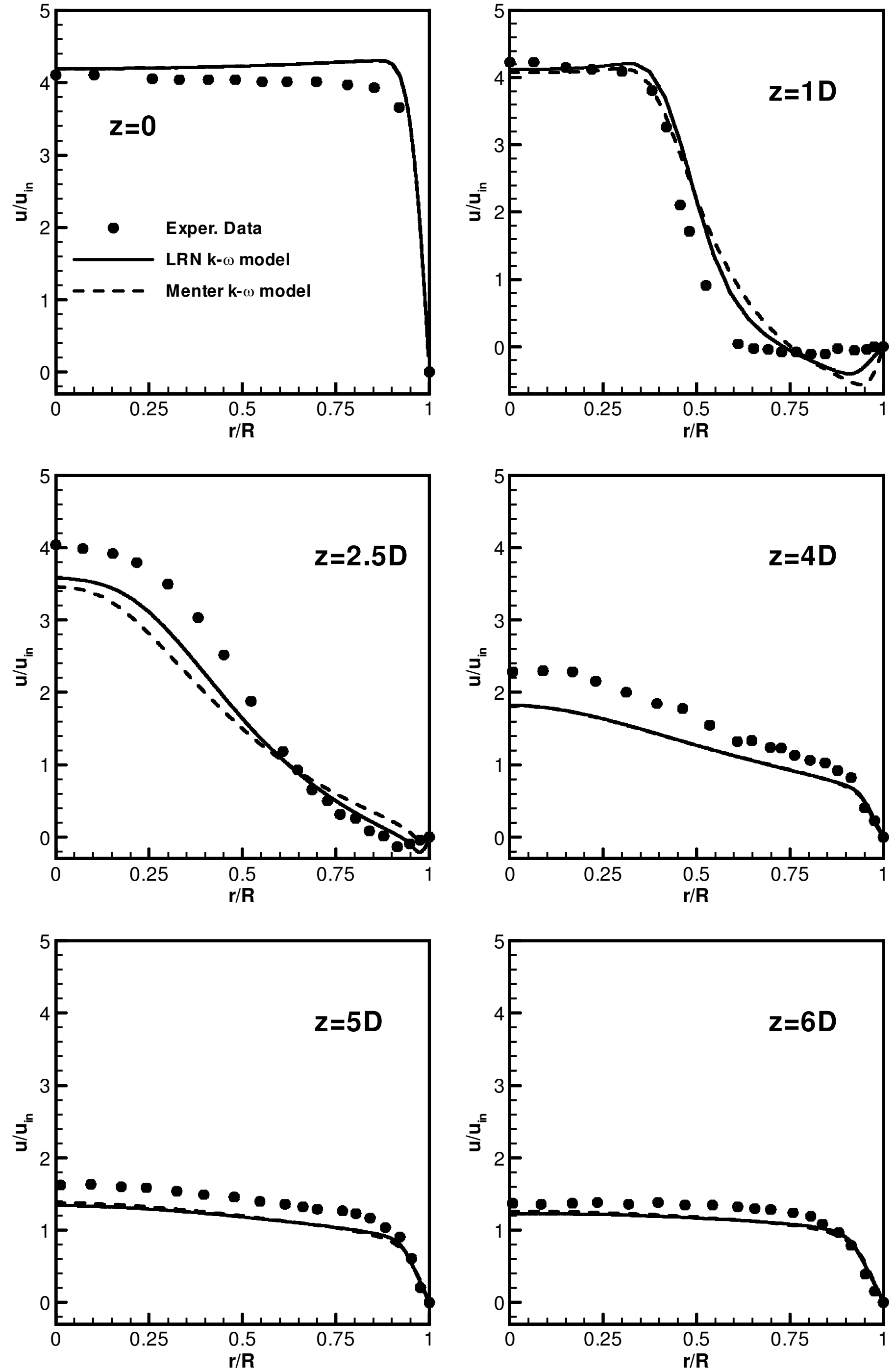

Fig. 6 Comparison of predicted axial velocity profiles at different axial locations for the constricted tube at $Re = 2 \times 10^3$ with experimental measurements of Ahmed and Giddens.[18]

throat for a 75% local occlusion. In this case the reattachment length is longer than that for the $Re = 2 \times 10^3$ case; it is about $5.5D$–$6.5D$. The full transition form laminar to turbulent flow occurs near the reattachment point, as indicated by the relatively blunt velocity profile at $z = 6D$ (Fig. 7). Again, the Menter k–ω model amplifies the turbulence behavior and fails to capture the correct velocity profiles in the transition regime from $z = 1D$ to $5D$, whereas the velocity profiles predicted with the LRN k–ω model agree well with the experimental data points. Similarly, the onset of turbulence near $z = 6D$ can increase the discrepancy between model simulations and experimental measurements as a result of the increasing experimental uncertainty.

Figure 8 depicts the profile of the turbulence intensity along the centerline in the stenotic tube for an inlet Reynolds number of 2×10^3. The present LRN k–ω model does predict the rapid rise of turbulence intensity after $z > 2.5D$ and then a slower decrease. This high disturbance level can be attributed to the transition into intense turbulence; indeed, the maximum turbulence level usually takes place in the vicinity of the flow reattachment point.[19] The predicted values and locations of the peak and near-peak flow fluctuations agree very well with the experimental results. However, elevated turbulence intensity levels are also predicted in the throat, which were not reported in Ahmed and Giddens' experimental work.[18,19] Nevertheless, Corcoran and Chigier[20] reported that high levels of axial turbulence intensity were found within one diameter downstream of the throat in their jet flow experiments with a constricted larynx model. The increase of turbulence kinetic energy from $z = -1D$ to 0, as shown in Fig. 8, can be attributed to the gradual constriction of the tube and the increase in local Reynolds number, that is, from 2×10^3 to 4×10^3. In contrast, with the expansion of the tube from

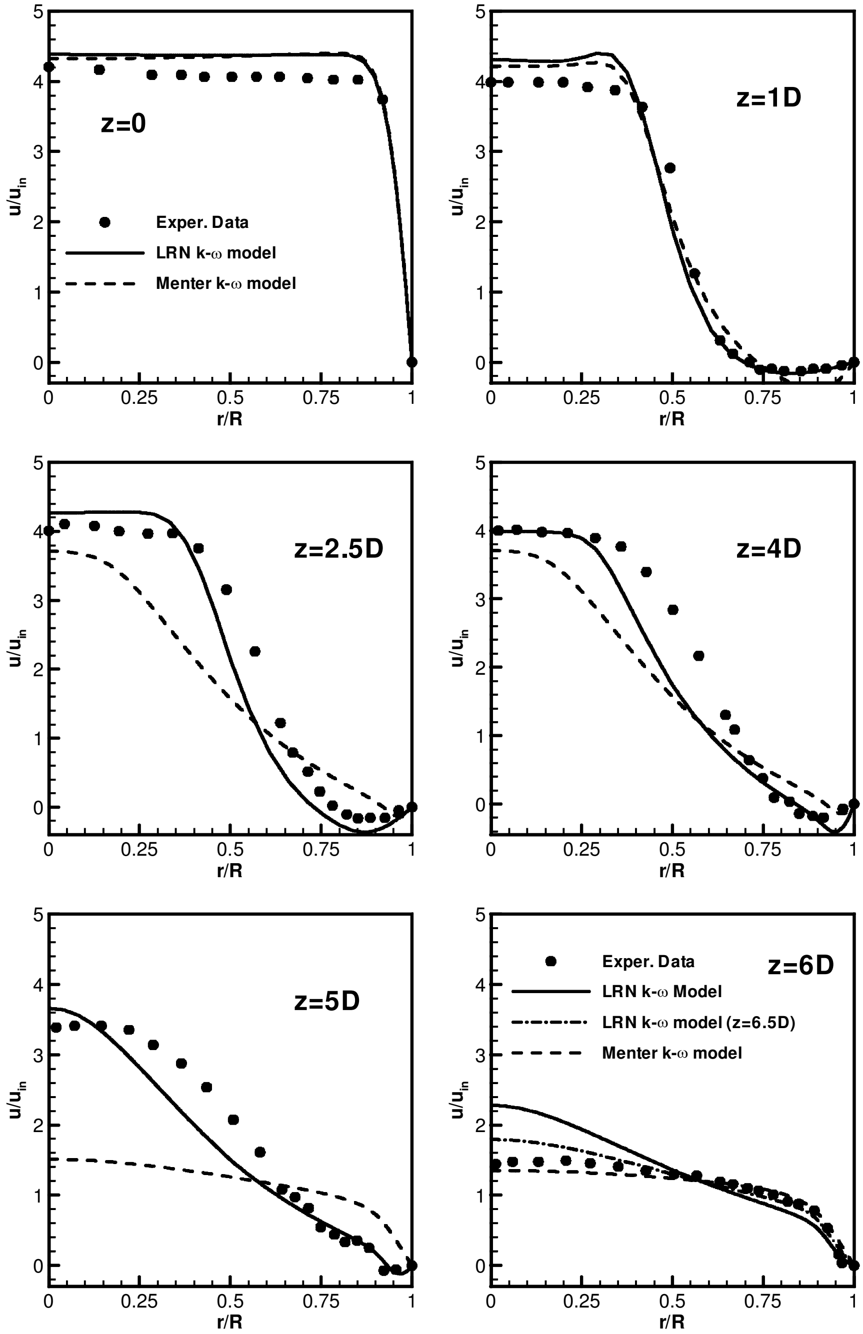

Fig. 7 Comparison of predicted axial velocity profiles at different axial locations for the constricted tube at $Re = 10^3$ with experimental measurements of Ahmed and Giddens.[19]

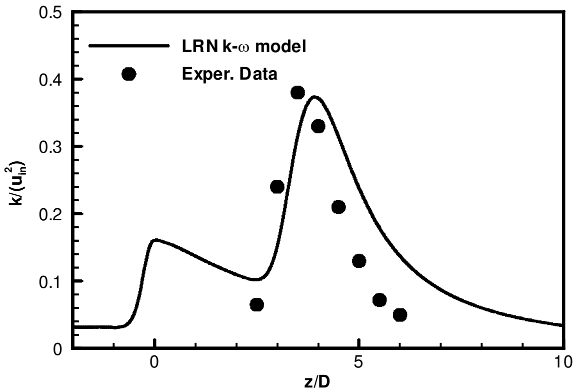

Fig. 8 Comparison of computed centerline turbulence intensity for the constricted tube at $Re = 2 \times 10^3$ with experimental measurements of Ahmed and Giddens.[19]

$z = 0$ to $1D$ the turbulence intensity can decrease somewhat until the transition starts.

Laminar-to-Turbulent Flow in the Oral-Airway Model

Accurate simulations of airflow structures in the oral airway are critical in predicting the transport and deposition of toxic particles or therapeutic aerosols in the human respiratory system.[21,22] As mentioned before, airflow in the human upper airways is mostly in the transitional flow regime; thus, it is likely that portions of the flow could be locally laminar, and other portions could be locally turbulent. A proper LRN turbulence model must be successful in predicting not only transitional and turbulent flow but also laminar flow. The ability of the LRN k–ω model to reproduce laminar flow behavior was further evaluated with an oral airway geometry (see Fig. 1b), assuming a low inspiratory flow rate of $Q_{\text{in}} = 10$ l/min. The maximum Reynolds number for this simulation was below 1.5×10^3 (see Fig. 2). The results of pressure drop and velocity profiles for the oral-airway geometry are shown in Figs. 9 and 10, where the LRN

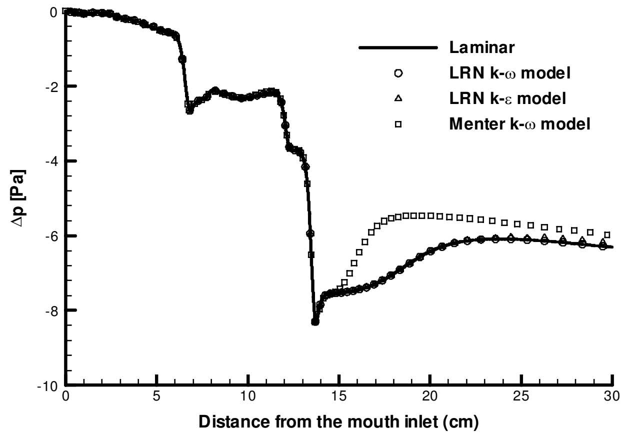

Fig. 9 Comparison of turbulence models predicting laminar flow pressure drops in the oral airway with an inspiratory flow rate of $Q_{\text{in}} = 10$ l/min.

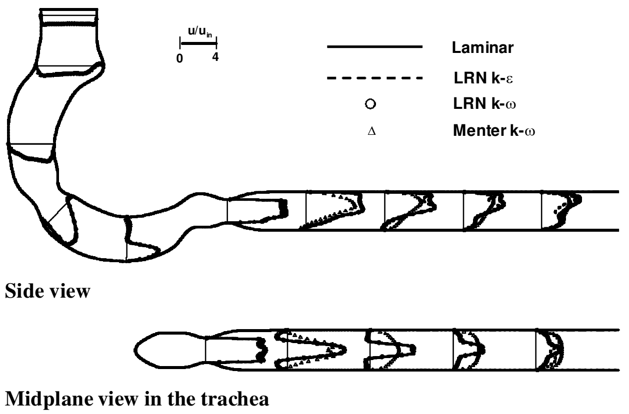

Fig. 10 Comparison of turbulence models predicting laminar velocity profiles in the oral-airway model with an inspiratory flow rate of $Q_{\text{in}} = 10$ l/min.

turbulence model predictions are compared to those for laminar flow. In Fig. 9 Δp is the pressure drop defined as $\Delta p = \bar{p} - p_{\text{in}}$, where $\bar{p}$ is the cross-sectional area-averaged pressure and p_{in} is the inlet pressure at the mouth. As expected, both the LRN k–ω and LRN k–ε model predictions match closely the laminar flow results. The Menter k–ω model prediction deviates from the laminar pressure drop after the constriction of the glottis because of its overestimation of flow instability for low-Reynolds-number flow. Similar results were observed for the velocity profiles (Fig. 10), that is, the LRN k–ω model predicts the laminar velocity field very well and the Menter k–ω model predicts the onset of turbulence after the throat even for laminar flow. However, the LRN k–ε model fails to predict laminar velocity profiles further downstream.

It can be concluded that the LRN k–ω model adopted here for internal flows appears to be capable of reproducing the limiting behavior of both laminar and fully turbulent flows and is appropriate to simulate the transitional flow in locally constricted conduits. In fact, the laminar flow behavior in the oral airway is depicted in Fig. 10 for the low inspiratory flow rate of $Q_{\text{in}} = 10$ l/min, where 1) the velocity profiles become skewed in the curved portion of the oral cavity and pharynx/larynx as a result of centrifugal effects; 2) flow separation occurs with abrupt geometric changes, that is, the variation of cross-sectional area in the lower portion of the mouth (near the tongue), the pharynx region after the soft palate, and downstream of the vocal fold (glottis); 3) flow is nearly uniform at the glottis; and 4) an asymmetric laryngeal jet is generated after the glottis.

Figures 11 and 12 show the mean velocity profiles and turbulence kinetic energy profiles in the human oral airway under normal breathing condition ($Q_{\text{in}} = 30$ l/min), that is, Re_{local} is between 1.5×10^3 and 5×10^3 (see Fig. 2). The cross-sectional views display the axial velocity contours as well as secondary velocity vectors in Fig. 11 and the contours of k/u_{in}^2 values in Fig. 12. The cross sections C–C′, D–D′, E–E′, and F–F′ are zero, one, three, and six diameter(s) from the glottis, respectively. The primary characteristics of the axial flowfields, including skewed flow in the curved pharynx region, recirculating flows and the laryngeal jet are clearly exhibited in Fig. 11 as well. From the cross-sectional views in Fig. 11, it can be seen that secondary motion was set up when

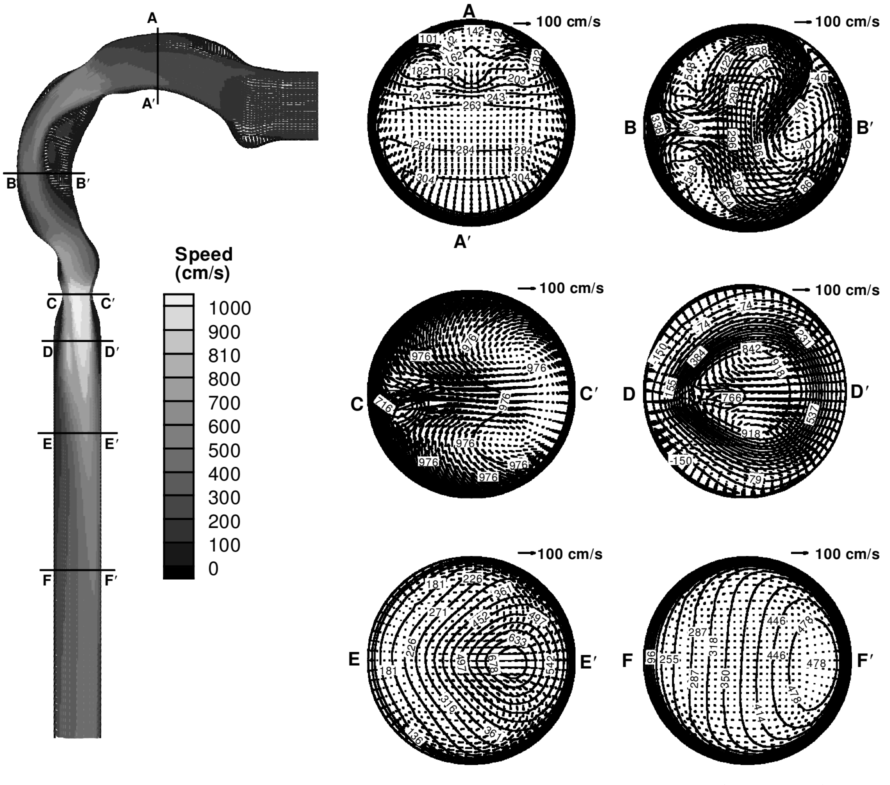

Fig. 11 Velocity fields in the oral-airway model for $Q_{\text{in}} = 30$ l/min. The left-hand panel exhibits midplane ($y = 0$ plane) velocity contours with uniform velocity vectors. The right-hand panel shows the axial velocity contours (magnitudes in centimeters per second) and secondary velocity vectors at different cross sections.

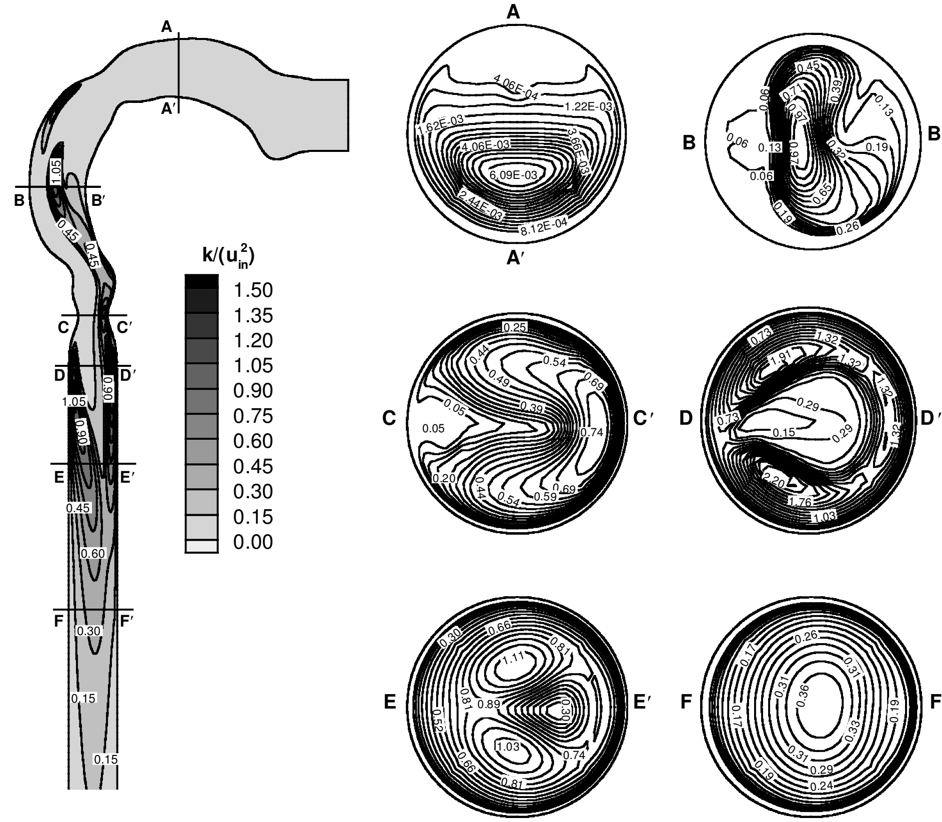

Fig. 12 Distribution of turbulence kinetic energy (k/u_{in}^2) in the oral-airway model for Q_{in} = 30 l/min. The left-hand panel is the side view ($y = 0$ plane), and the right-hand panel provides the cross-sectional views.

the flow turns a bend from the mouth to the pharynx because of the centrifugally induced pressure gradient. The intensity of secondary flow is strong in the curved pharynx region, but it decreases after the glottis with the onset of turbulence, and it eventually becomes very weak at cross section F–F′ (six diameters from the glottis). At the same time, with the redistribution of the kinetic energy of the flow over most of the cross section the velocity profile become more blunt from the left to the right wall, and the maximum velocity zone moves to the anterior wall (F′) at the cross section F–F′.

The turbulence intensity is still very weak at the initial part of the oral airway (Fig. 12); however, it rises rapidly after the constriction caused by the soft palate, and then decreases until the disturbance is activated again by the throat (glottis). The maximum turbulence fluctuations occur in the shear layer rather than around the centerline after the glottis. This phenomenon indicates that the flow first becomes unstable in the region of the shear layer bounding the jet emerging from the throat.[23] A general trend in turbulence generation and decay after the glottis is apparent. Turbulence levels seem to increase quickly through the 0–2.5 diameter zone after the glottis, and then decay approaching an asymptotic level of approximately 0.2–0.3 at six-diameter station from the throat (cross section F–F′), which is similar to that in the constricted tube discussed in the preceding section. High levels of turbulence intensity can be observed in Fig. 12 near the posterior/left and posterior/trachea wall from 0.5 to 2.0 diameters downstream of the glottis. These regions with strong flow fluctuations might indicate a high potential for tracheal deposition of small particles.[24]

Conclusions

Four widely used turbulence models, that is, the low-Reynolds-number (LRN) k–ω model, LRN k–ε model, RNG k–ε model, and Menter k–ω model, are compared with respect to their merits to predict laminar, transitional, and turbulent flows in a straight tube with a 75% smooth constriction and an oral-airway model with bends and partial occlusions. Both the RNG k–ε and Menter k–ω models amplify the flow instabilities after the constrictions and hence fail to capture the laminar flow behavior at low Reynolds numbers. The LRN k–ε model fails to simulate the transition to turbulent flow, and it requires relatively high computational resources. The LRN k–ω model adopted for complex three-dimensional tubular flows in this study appears to be capable of reproducing the behavior of laminar, transitional, and fully turbulent flows. Moreover, the LRN k–ω model predicts the maximum turbulence fluctuations quite well, which is very important in considering the rapidly changing airflow structures and the turbulent dispersion of particles. Hence, it can be concluded that the LRN k–ω model is appropriate to simulate laminar-transitional-turbulent flows in constricted tubes, such as the human upper airways, stenosed blood vessels, obstructed pipes, etc.

Acknowledgments

This effort was sponsored by the U.S. Air Force Office of Scientific Research, U.S. Air Force Material Command, under Grant F49620-01-1-0492 (Walt Kozumbo, Program Manager) and the National Science Foundation (BES-0201271; Gil Devey, Program Director). The U.S. Government is authorized to reproduce and distribute reprints for governmental purposes notwithstanding any copyright notation thereon. The use of CFX software from AEA Technology (Pittsburgh, Pennsylvania) and access to the SGI Origin 2400 workstation at the North Carolina Supercomputing Center (Research Triangle Park, North Carolina) are gratefully acknowledged as well. The views and conclusions contained herein are those of the authors and should not be interpreted as necessarily representing the official policies or endorsements, either expressed or implied, of the U.S. Air Force Office of Scientific Research or the U.S. Government.

References

[1] Lakshminarayana, B., "Turbulence Modeling for Complex Shear Flows," *AIAA Journal*, Vol. 24, No. 12, 1986, pp. 1900–1917.

[2] Han, Z., and Reitz, R. D., "Turbulence Modeling of Internal Combustion Engines Using RNG k–ε Models," *Combustion Science and Technology*, Vol. 106, No. 4–6, 1995, pp. 267–295.

[3] Katz, I. M., Martonen, T. B., and Flaa, W., "Three-Dimensional Computational Study of Inspiratory Aerosol Flow Through the Larynx: The Effect of Glottis Aperture Modelation," *Journal of Aerosol Science*, Vol. 28, No. 6, 1997, pp. 1073–1084.

[4] Papageorgakis, G. C., and Assanis, D. N., "Comparison of Linear and Nonlinear RNG-Based k–ε Models for Incompressible Turbulent Flows," *Numerical Heat Transfer Part B*, Vol. 35, No. 1, 1999, pp. 1–22.

[5] Renotte, C., Bouffioux, V., and Wilquem, F., "Numerical 3D Analysis of Oscillatory Flow in the Time-Varying Laryngeal Channel," *Journal of Biomechanics*, Vol. 33, No. 12, 2000, pp. 1637–1644.

[6] Stapleton, K. W., Guentsch, E., Hoskinson, M. K., and Finlay, W. H., "On the Suitability of k–ε Turbulence Modeling for Aerosol Deposition in the Mouth and Throat: A Comparison with Experiment," *Journal of Aerosol Science*, Vol. 31, No. 6, 2000, pp. 739–749.

[7] Wilcox, D. C., *Turbulence Modeling for CFD*, 2nd ed., DCW Industries, Inc., La Canada, CA, 1998, pp. 103–217.

[8] Menter, F. R., "Two-Equation Eddy-Viscosity Turbulence Models for Engineering Applications," *AIAA Journal*, Vol. 32, No. 8, 1994, pp. 1598–1605.

[9] Jones, W. P., and Launder, B. E., "Calculation of Low-Reynolds-Number Phenomena with a Two-Equation Model of Turbulence," *International Journal of Heat and Mass Transfer*, Vol. 16, No. 6, 1973, pp. 1119–1130.

[10] Launder, B. E., and Sharma, B. I., "Application of the Energy Dissipation Model of Turbulence to the Calculation of Flow near a Spinning Disc," *Letters in Heat and Mass Transfer*, Vol. 1, No. 2, 1974, pp. 131–138.

[11] Lam, C. K. G., and Bremhorst, K. A., "Modified Form of k–ε Model for Predicting Wall Turbulence," *Journal of Fluids Engineering*, Vol. 103, No. 3, 1981, pp. 456–460.

[12] Chien, K.-Y., "Prediction of Channel and Boundary-Layer Flows with a Low-Reynolds-Number Turbulence Model," *AIAA Journal*, Vol. 20, No. 1, 1982, pp. 33–38.

[13] Kral, L. D., "Recent Experience with Different Turbulence Models Applied to the Calculation of Flow over Aircraft Components," *Progress in Aerospace Sciences*, Vol. 34, No. 7–8, 1998, pp. 481–541.

[14] Radmehr, A., and Patankar, S. V., "Computation of Boundary Layer Transition Using Low-Reynolds-Number Turbulence Models," *Numerical Heat Transfer*, Vol. 39, No. 6, 2001, pp. 525–543.

[15] Hill, P., and Peterson, C., *Mechanics and Thermodynamics of Propulsion*, 2nd ed., Addison Wesley Longman, Reading, MA, 1992, pp. 137–466.

[16] LeFebvre, A. W., *Gas Turbine Propulsion*, McGraw–Hill, New York, 1983.

[17] AEA Technology, *CFX-4.4: Solve*, CFX International, Oxfordshire, U.K., 2001, pp. 1–877.

[18] Ahmed, S. A., and Giddens, D. P., "Velocity Measurements in Steady Flow Through Axisymmetric Stenoses at Moderate Reynolds Number," *Journal of Biomechanics*, Vol. 16, No. 7, 1983, pp. 505–516.

[19] Ahmed, S. A., and Giddens, D. P., "Flow Disturbance Measurements Through Constricted Tube at Moderate Reynolds Number," *Journal of Biomechanics*, Vol. 16, No. 12, 1983, pp. 955–963.

[20] Corcoran, T. E., and Chigier, N., "Characterization of the Laryngeal Jet Using Phase Doppler Interferometry," *Journal of Aerosol Medicine*, Vol. 13, No. 2, 2000, pp. 125–137.

[21] Comer, J. K., Kleinstreuer, C., and Kim, C. S., "Flow Structures and Particle Deposition Patterns in Double Bifurcation Airway Models. Part 2. Aerosol Transport and Deposition," *Journal of Fluid Mechanics*, Vol. 435, 2001, pp. 55–80.

[22] Zhang, Z., and Kleinstreuer, C., "Transient Airflow Structures and Particle Transport in a Sequentially Branching Lung Airway Model," *Physics of Fluids*, Vol. 14, No. 2, 2002, pp. 862–880.

[23] Yongchareon, W., and Young, D. F., "Initiation of Turbulence in Models of Arterial Stenoses," *Journal of Biomechanics*, Vol. 12, No. 3, 1979, pp. 185–196.

[24] Schlesinger, R. B., and Lippman, M, "Particle Deposition in the Trachea: In Vivo and In Hollow Casts," *Thorax*, Vol. 31, No. 6, 1976, pp. 678–684.

R. M. C. So
Associate Editor